OPEN ACCESS
IOP Publishing
Journal of Physics D: Applied Physics
J. Phys. D: Appl. Phys. 58 (2025) 155204 (19pp)
https://doi.org/10.1088/1361-6463/adb9f6

Control of core–shell nanoparticles properties through plasma synthesis: a computational study

Yifan Gui[1], **Eve Lanham**[2] **and Mark J Kushner**[3,*]

[1] Nuclear Engineering and Radiological Sciences Department, University of Michigan, 2355 Bonisteel Blvd, Ann Arbor, MI 48109, United States of America
[2] Chemical Engineering Department, University of Michigan, 2300 Hayward St, Ann Arbor, MI 48109, United States of America
[3] Electrical Engineering and Computer Science Department, University of Michigan, 1301 Beal Ave, Ann Arbor, MI 48109-2122, United States of America

E-mail: mjkush@umich.edu, evangyf@umich.edu and sjlanham@umich.edu

Received 22 December 2024, revised 23 January 2025
Accepted for publication 25 February 2025
Published 5 March 2025

Abstract

The improved properties of core–shell nanoparticles (CSNPs) over homogeneous nanoparticles (NPs) have expanded and diversified the applications of these nanomaterials. However, controlling the properties of CSNPs can be a challenging task. Low temperature plasmas have proven to be an effective method of producing NPs with uniform size and morphology, and high yield. That said, NP transport and growth dynamics are sensitive to LTP properties. We report on a computational investigation of the evolution of Ge–Si CSNP properties as a function of operating conditions through the modeling of a flowing, two-zone inductively coupled plasma (ICP) reactor. Ar/GeH_4 and Ar/SiH_4 gas mixtures were supplied to separate plasma zones at a pressure of 1 Torr to promote growth of Ge cores and Si shells. The negatively charged CSNPs are trapped electrostatically in the vicinity of the antennas where the plasma is generated and where the majority of particle growth occurs. Particles that grow to a critical size are then de-trapped by fluid drag due to neutral gas flow. A two-dimensional hybrid plasma model coupled with a three-dimensional kinetic NP transport model were utilized to resolve plasma chemistry and NP growth processes that take place on distinct timescales. The trends in CSNP properties and trapping mechanisms associated with flow rate, applied ICP power and inlet precursor fraction are discussed. While the spatial distribution of plasma produced radical species can have significant impact on the NP growth process, the NP transport dynamics are what ultimately dictates the growth environment that is unique to each particle and so determines their final dimension and composition. The key to optimizing reactor conditions involves controlling the spatial density of growth species and plasma profile as a means to tailor particle trapping dynamics suitable to produce CSNPs for a specific application.

---

[*] Author to whom any correspondence should be addressed.

Supplementary material for this article is available online

Keywords: nanoparticles, plasmas, core–shell, plasma synthesis, model

1. Introduction

Synthesis of core–shell nanoparticles (CSNPs) has been a focus of research in applications of nanotechnology. CSNPs potentially have multifunctional capabilities that homogeneous nanoparticles (NPs) are not able to achieve. Characterized by an architecture that consists of an inner core encapsulated by an outer shell, these heterostructured CSNPs can be made with a wide variety of material combinations to provide diverse properties such as improved stability, biocompatibility, magnetic behavior, catalytic activity, and optical characteristics [1–4]. The concept of CSNPs was inspired by the need to enhance the performance of materials at the nanoscale for a broad spectrum of applications. By selecting and optimizing the core and shell materials and dimensions (typically in the sub-10 nm diameter range), researchers are able to tailor these NPs to suit application requirements in semiconductor [5–8], biomedicine [9–11] and catalyst [12, 13] disciplines. For example, their low-toxic nature and high chemical and thermal stability enables CSNPs to be used for targeted drug delivery [14] and biological labeling [11, 15] while their desirable optoelectronic properties are being leveraged, for example, as solar cell concentrators [16–18]. Ge–Si CSNPs have been investigated as potential candidates for floating gate material in metal oxide semiconductor field effect transistors [19, 20], doping of solar cells [21], and as a thermoelectric material [22].

Tailoring of CSNPs for specific applications requires precise control over their size, shape, and composition. While NPs with diameters of tens of nanometers can exhibit quantum confinement due to the formation of discrete energy levels, introducing a shell around these NPs provides chemical stability and limits non-radiative recombination events that reduce photoluminescence [23]. The degree of core and shell purity, and the transition between core-and-shell, affects carrier confinement and results in varying levels of photoluminescence quantum yield (PLQY), an important performance metric for bioimaging and LED technologies. Impurities alter the relative band alignment between the two components and create trap states that quench fluorescence and degrade PLQY [24].

Plasma synthesis of NPs and CSNPs leverages a non-equilibrium, low pressure plasma processing environment that has several potential advantages over traditional fabrication techniques such as solution-based synthesis [25]. It is possible to modify NP properties (size, morphology, composition) through tuning plasma reactor operating parameters such as gas composition and flow rate, applied power, pulsing and pressure [26–28]. Due to the high mobility of negatively charged electrons in low temperature plasmas (LTPs) compared to positively charged ions, NPs with radii greater than a few nanometers will negatively charge. The mutual repulsion between negatively charged NPs lessens the likelihood of coagulation, resulting in a monodisperse NP size distribution. In the non-equilibrium plasma environment, electrons have average energies of a few eV while the gas has temperatures near ambient. The growing NPs interact with the electrons and ions, and plasma produced radicals through surface reactions (ion-electron recombination, radical attachment) that can heat the NPs to temperatures exceeding the ambient, leading to annealing and crystallization of NPs. This *in-situ* annealing of, for example, group IV semiconductor materials (Si, Ge) provides some advantages over liquid-based synthesis [8]. However, excessive heating of NPs in high plasma density systems can result in particle evaporation and suppression of NP growth [29].

The high efficiency of direct gas to particle conversion in plasmas translates to a higher NP yield in plasma synthesis. However, controlling NP properties through tuning of multiple plasma process parameters is difficult. Minor variations in operating conditions can result in significant changes in plasma properties which in turn impact NP properties. Therefore, establishing relationships between plasma process parameters and NP properties would be beneficial to improving plasma reactor and recipe design for novel nanomaterial production.

Radio-frequency (rf) and DC plasma reactor configurations have been investigated to produce NPs. Typical conditions are a cylindrical plasma tube of 1–2 cm diameter, with a few to tens of Watts of power deposition, sustaining a plasma in a few Torr of a flowing gas having a residence time of up to tens of ms. The gas composition is usually a rare gas (such as argon) with at most a few percent of the NP precursor species [8, 28, 30–32]. For Ge–Si CSNP synthesis, small fractions of germane (GeH_4) or germanium tetrachloride ($GeCl_4$) in an argon or helium carrier gas are used to produce germanium cores while silane (SiH_4) or silicon tetrachloride ($SiCl_4$) serve as precursors for shell growth [8, 26]. The electron impact dissociation of these precursor gases occurs rapidly in the vicinity of the plasma zone to produce radicals that facilitates NP formation through nucleation and surface growth [33].

Synthesis of Ge–Si CSNPs using a cylindrical, flowing capacitively coupled plasma (CCP) was experimentally demonstrated by Hunter *et al* [8]. The reactor used a single CCP source operating at 50 W and 13.56 MHz. Ar/$GeCl_4$ was introduced above the plasma source to synthesize Ge cores and the Si shell was produced by flowing in a Ar/SiH_4 mixture downstream. Collected CSNPs had a Ge core radius of approximately 4 nm and Si shell thickness of 1–4 nm depending on the silane fraction (1%–5%). Hunter *et al* also produced Si-SiN_x CSNPs using a cylindrical dual-source CCP system [28].

$Ar/SiH_4/H_2$ was flowed through the upper plasma zone, producing Si cores while Ar/NH_3 was introduced near the lower plasma zone to promote surface nitridation of the Si cores. The reactor produced CSNPs with small cores of roughly 1 nm in radius, a consequence of the higher gas flow speed that limited residence time in the plasma zone.

Particle charging in LTPs is among the more important mechanisms that underly plasma synthesis of NPs. The extent to which a NP can be charged is a function of particle diameter, capacitance and current to the surface of the particle. Negatively charged NPs experience electrostatic forces and tend to be trapped in regions of positive plasma potential where surface growth can occur for an extended period [34]. The strength and spatial profile of these electrostatic traps affect particle residence time and, in principle, can be tailored to produce CSNPs having desired properties.

In this paper, we report on results from a computational investigation of Ge–Si CSNP synthesis in a flowing LTP system. The goal of this work is to quantify the impact of operating parameters on particle trapping, the resulting CSNP dimensions and composition, and so provide a guide for experimentally customizing CSNP properties. Simulations were performed of a cylindrical two-coil inductively coupled plasma (ICP) reactor with an Ar/GeH_4 gas mixture supplied from a top inlet into the primary ICP zone for germanium core production and an Ar/SiH_4 gas mixture supplied from a downstream inlet into the secondary ICP zone for producing the silicon shell over the germanium cores. The reactor operated with a pressure of 1 Torr, ICP power of 5–20 W, and inlet SiH_4 mole fraction of 0.5%–20%. The modeling platforms used in this work are a two-dimension plasma hydrodynamics model coupled with a three-dimensional kinetic dust particle transport simulator for particle trajectory, growth and composition tracking. Sticking coefficient of small silicon hydride radicals were obtained from molecular dynamics simulations [35, 36].

The emergence of several particle trapping modes occurred under specific reactor conditions. These modes are characterized by distinct particle trapping locations and residence time in each plasma zone (primary and secondary) as a result of the dynamically changing NP charge and diameter. Other than CSNPs having different core-to-shell ratio and diameters, the core and shell purity (atomic fraction of germanium in core and silicon in shell) were also influenced by variations in the spatial distribution of growth species.

The modeling platforms used in this work are described in section 2. Particle dynamics, size distribution and core and shell purity as a result of varying inlet flow rate, applied ICP power, and inlet silane fraction are discussed in section 3. Concluding remarks are in section 4.

2. Description of the models

The reactor scale plasma chemistry was simulated using the 2-dimensional (2D) plasma hydrodynamics model hybrid plasma equipment model (HPEM). NP particle transport and growth was addressed by the dust transport simulator (DTS) in conjunction with the HPEM. Sticking coefficient of small silicon hydride species used were computed by colleagues using the LAMMPS molecular dynamics simulation platform [35, 36].

2.1. Reactor scale model and plasma chemistry

The 2D reactor scale plasma chemistry was addressed by the HPEM, a collection of modules that interact synergistically to simulate physical processes in LTPs, described in detail in [37]. Modeling of the ICP investigated here utilized the electromagnetics module (EMM) of the HPEM that solves the frequency domain wave equation, derived from Maxwell's equations, producing spatially varying electric and magnetic fields, and power deposition. The trajectories of electrons produced by secondary emission from surfaces resulting from ion bombardment were computed by the electron energy transport module (EETM) using Monte Carlo techniques. The EETM also generates electron impact rate coefficients for bulk electrons by solving Boltzmann's equation using a 2-term spherical harmonic expansion to produce electron energy distributions. The combined outputs from EMM and EETM, were utilized by the fluid kinetics-Poisson module to determine neutral and charged species densities, momenta and temperatures. At pressures of a few Torr, a drift-diffusion approximation was used when solving electron continuity and temperature equations. Poisson's equation was solved semi-implicitly to produce electrostatic fields, which are used for particle transport and in the EETM. These quantities are cycled back to other modules.

A hierarchical reaction mechanism of silicon and germanium chemistry was developed to enable modeling of CSNP synthesis. The fundamental Ar/SiH_4 chemistry was based on the work of Picard *et al* [38] with additional data from previous studies [35, 36]. Germanium chemistry was replicated from the silicon chemistry due to the lack of experimental data, while transport coefficients considered the mass of the germanium hydride molecules. Building upon the previous mechanism, the current reaction set involves silicon and germanium hydride species up to $Si_{12}H_{26}$ and $Ge_{12}H_{26}$. The large silicon and germanium hydride species were categorized as either saturated (Si_xH_{x+2}, Ge_xH_{x+2}) or unsaturated/radical (Si_xH_{x+1}, Ge_xH_{x+1}). Multiple radical species (Si_xH_y, $y = 1$ to $x + 1$) with the same number of Si or Ge were binned into a single species for computational efficiency. For example, Si_3H_7 in the model contains species Si_3 to Si_3H_7. Reaction rate coefficients and sticking coefficients for the radicals were estimated based on the sum of all sub-radicals under the main radical species for clusters or molecules having the same number of Si or Ge atoms.

The availability of dangling bond/free radical sites enables unsaturated species to stick onto NPs for surface growth whereas the saturated counterparts are unreactive at low temperatures. The species included in the reaction mechanism are listed in table 1. The hierarchy of silicon and germanium hydride species was chosen to end at $x = 13$, a point where the molecules have sizes large enough to be considered NPs. At this cluster size, surface reactions such as sticking of radicals become the dominant growth processes of the particle.

Table 1. Species in the reaction mechanism.

Argon species and electrons
Ar, Ar($1s_5$), Ar($1s_4$), Ar($1s_3$), Ar($1s_2$), Ar(4p), Ar(4d), Ar_2^*, Ar^+, Ar_2^+, ArH^+, e
Hydrogen species
H, H^*, H_2, H_2^*, H^+, H_2^+, H_3^+, H^-
Silicon hydride species
SiH, SiH_2, SiH_3, SiH_4, Si_2H_2, Si_2H_3, Si_2H_5, Si_2H_6, Si_xH_{x+1}, Si_xH_{x+2} (x=3−12), SiH^+, SiH_2^+, SiH_3^+, $Si_2H_2^+$, $Si_2H_5^+$, $Si_2H_6^+$, $Si_xH_{x+1}^+$, $Si_xH_{x+2}^+$ (x=3−6), SiH_2^-, SiH_3^-, $Si_2H_3^-$, $Si_2H_5^-$
Germanium hydride species
GeH, GeH_2, GeH_3, GeH_4, Ge_2H_2, Ge_2H_3, Ge_2H_5, Ge_2H_6, Ge_xH_{x+1}, Ge_xH_{x+2} (x=3−12), GeH^+, GeH_2^+, GeH_3^+, $Ge_2H_2^+$, $Ge_2H_5^+$, $Ge_2H_6^+$, $Ge_xH_{x+1}^+$, $Ge_xH_{x+2}^+$ (x=3−6), GeH_2^-, GeH_3^-, $Ge_2H_3^-$, $Ge_2H_5^-$

Table 2. Sticking coefficient of radicals onto NPs.

Species	S_c
SiH_3/GeH_3	0.125
SiH_2/GeH_2	0.66
SiH/GeH	0.945
Si_2H_2/Ge_2H_2	0.66
Si_2H_3/Ge_2H_3	0.3
Si_2H_5/Ge_2H_5	0.1
Si_xH_y/Ge_xH_y (x=3−12, y=1 to x−1)	0.5

The computation of SiH_x (x = 1–3), Si_2H_2, Si_2H_3, Si_2H_5 sticking coefficients S_c were performed by LAMMPS molecular dynamics simulation [39, 40]. The sticking coefficients of larger silicon and germanium hydrides were approximated based on the average free radical site availability of the members in the unsaturated hydride of a given size. The sticking coefficients of radicals are summarized in table 2. The additional reaction mechanism of large hydrides is listed in Supplementary Material.

2.2. NP transport in the DTS

The DTS is a kinetic model coupled to HPEM to generate three-dimensional particle trajectories of NPs in the plasma reactor while accounting for particle growth and charging. The current implementation of the DTS is based on prior versions of the DTS [27]. The detailed workflow of the DTS is described in [27], and a brief description is given here. On each call to the DTS, the HPEM provides the spatial distribution of species temperatures, densities, neutral and ion momenta, and electric fields. NP nucleation is not modeled by the DTS but instead, seed NPs (10 000 for this work) were randomly sited in regions where nucleation events are likely to occur based on the results of the HPEM. These seed NPs then grow through sticking of radical species onto the surface or by agglomeration, though the contribution of agglomeration is small due to the charging of the NPs. Radical species densities required for calculation of growth rates are interpolated from values at numerical mesh points provided by the HPEM. The growth rate of NPs is

$$\frac{\mathrm{d}m_{\mathrm{NP}}}{\mathrm{d}t} = \sum_i 4\pi r_{\mathrm{NP}}{}^2 \Gamma_i S_{c,i} \triangle m_i \tag{1}$$

where m_{NP} and r_{NP} are the mass and radius of a NP. Addition of mass comes from radical species i that has incident flux Γ_i, sticking coefficient S_c and mass $\triangle m_i$. The growth rate is then integrated through time to track particle mass, radius, density and volume. The DTS does not track the surface coverage of physiosorbed or chemisorbed species, which could result in an overestimation of NP growth rates under ICP conditions. The agglomeration algorithm allows two NPs to combine if the sum of their particle radii is greater than the distance between those two particles. Mass and momentum are conserved during the agglomeration process. The NP radius is derived from the updated particle mass and the average mass density while assuming the new particle remains spherical in shape. Surface reactions such as ion recombination or radical recombination produce heating of the NPs which can have a significant impact on the growth process under specific conditions (e.g. high plasma density, low thermal conductivity of the carrier gas). Particle temperature can increase to the point that NP growth is impeded by evaporation [29]. Particle heating is not addressed in this study.

For particles having diameters in the nanometer (nm) range, current collection at the particle surface resulting in NP charging is computed by using orbit motion limited theory. For small particles with sizes of a few nm, a stochastic charging algorithm was implemented to prevent non-integer number of charges accumulating within an integration timestep as might occur with a continuous charging process. The stochastic algorithm utilizes the mean expected value of a Poisson distribution to determine charge collection within a timestep. NPs in LTPs are usually negatively charged due to electrons having higher mobility than positive ions, however in this statistical approach, small particles that might support only a few charges may occasionally be neutral or even positively charged.

Through dynamically tracking particle mass, size and charge, the fundamental forces of electrostatic, gravitational, thermophoretic, ion drag, fluid drag force and interparticle Coulombic forces are considered. The formulation of these forces used in the model is described in [27]. Briefly, several factors determine the magnitude of these forces on a given NP, and in particular the size of the particle affects the strength of the forces. In addition to this scaling, each force has unique dependence on plasma properties which vary with position in the reactor. For example, the electric field strength and ion flux determine the strength of electrostatic and ion drag forces, whereas then temperature gradient and neutral gas velocity dictate the magnitude of thermophoretic and viscous fluid drag forces. Assuming the particles are charged negatively, electrostatic forces act in the direction opposite that of the electric field and ion drag force points in the direction of positive ion flux which usually flows away from the peak in plasma potential toward boundaries in the direction of the electric field. Regardless of particle charge, viscous fluid drag forces point in the direction of the neutral gas velocity and the thermophoretic force accelerates particles against the temperature gradient (from hotter to colder regions). The forces that determine the trajectory of a NP through the reactor change with diameter of the NP and the location of the NP in the reactor.

A composition tracking capability was developed for the DTS to predict the purity of the core and shell components of the CSNPs as they traverse different regions of the reactor. Similar to the particle growth algorithm, the mass fluxes of distinct materials contributing to growth of the NPs are collected to determine the atomic fraction of that material at each timestep, which are then integrated to provide the final core and shell compositions. The transition between growth of the core and shell occurs when the contributions from germanium and silicon exceed or fall below 50%. For some operating conditions in which these contributions do not cross 50% (for example, if Ge dominates growth throughout the reactor), then the location of the core to shell transition is set to be midway through the reactor (5 cm height). Integration of the instantaneous growth contributions from germanium and silicon enables the final core and shell purities to be determined.

The NP growth and particle tracking algorithms used in the investigation have weaknesses and strengths. This study couples the 3-dimensional kinetic DTS with the 2D HPEM. In doing so, the plasma properties from the HPEM that are used in the DTS are assumed to be azimuthally symmetric. Any azimuthal asymmetries in particle properties are then averaged when coupling back to the HPEM. Both of these practices are approximations. In experiments, the density of NPs may exceed 10^8–10^9 cm^{-3} which far exceeds the capability of the DTS to kinetically track individual NP particles. Consequently, the limit on the number of NPs can lead to overprediction of particle growth rates and charge as the depletion of growth species and electrons are likely lower in the simulation when compared to actual experiments with higher NP densities. Due to the inclusion of interparticle Coulombic interactions, the computation time in the DTS roughly scales with the square of the NP number. For the conditions discussed here, the integrated HPEM and DTS required 1–2 d to complete for one case with 10 000 particles.

3. Core/shell NP dynamics and composition tracking in flowing ICPs

3.1. Base case

The impacts of operating parameters including flow rate, inlet gas fraction and applied power on NP dynamics and core/shell purity were investigated. Plasma synthesis of NPs in similar reactor designs as used here has been demonstrated in several studies [28, 41–43] using either CCP or ICP sources. The tradeoffs of using either CCP or ICP are discussed in the conclusions section 4. An ICP reactor was chosen for this work due to the more defined plasma potential profile and quiescent nature of the plasma in ICPs compared to CCPs. The reactor is a cylinder consisting of two plasma zones generated by separate antennae sets to create upper and lower plasma zones for core and shell synthesis, as shown in figure 1(a). The cylindrical glass reactor spans 10 cm in height and 1.75 cm in radius. Both the top inlet and the pump were treated as metals to serve as electrical grounds. Ar/GeH$_4$ = 98/2 was flowed from the top inlet at 50 sccm to facilitate germanium core growth in the upper plasma zone and Ar/SiH$_4$ = 98/2 was supplied from the middle inlet at 20 sccm for silicon shell growth in the lower plasma zone. A lower middle inlet flow rate was chosen to extend the particle residence time in the vicinity of the second coil to accommodate growth of thicker shells. The pressure was kept at 1 Torr by throttling the outflow and the wall temperature was held constant at 325 K.

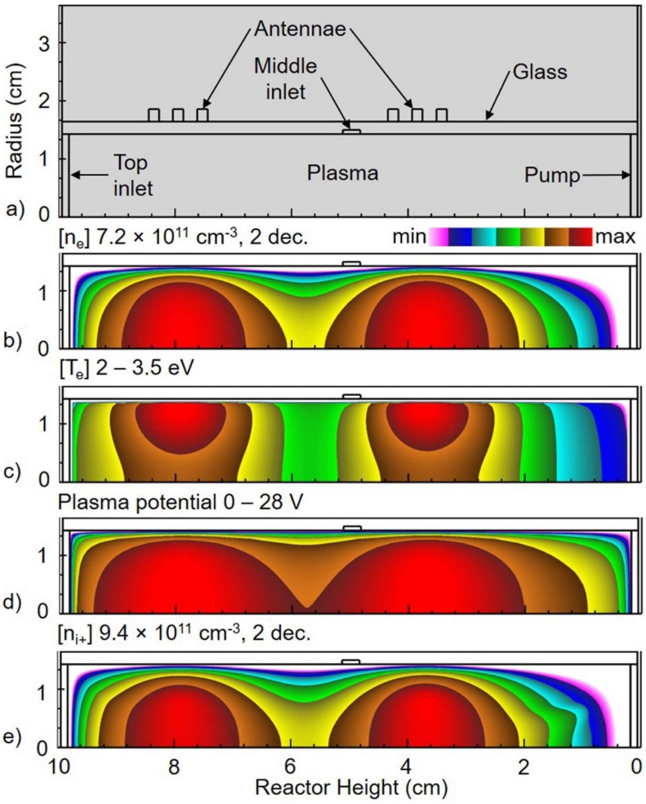

Figure 1. Reactor configuration and plasma properties for base case condition of 1 Torr. The top and bottom coil sets are individually powered at 10 W. Ar/GeH$_4$ = 98/2 at 50 sccm is flowed through the top inlet. Ar/SiH$_4$ = 98/2 at 20 sccm is flowed through the middle inlet. (a) Reactor configuration, (b) electron density, (c) electron temperature, (d) plasma potential and (e) positive ion density. Maximum value or range of values plotted is noted in each image. 2 dec indicates the number of decades of the log-scale plot.

Plasma properties are shown in figure 1 for the base case conditions. The electron density peaks on axis adjacent to the antenna at 7.2 × 10^{11} cm^{-3} and decays by two orders of magnitude moving away from the antennae region due to increasing rates of electron impact dissociative attachment

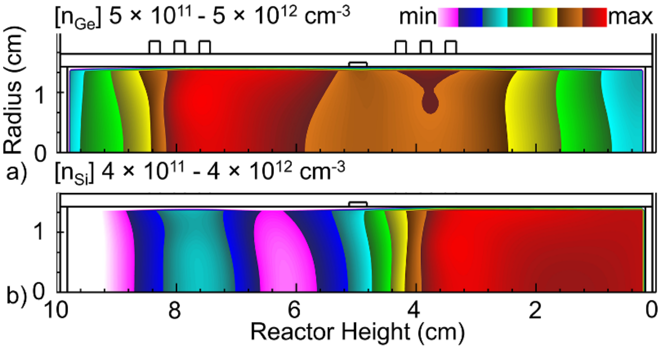

Figure 2. Density of (a) germanium and (b) silicon growth species weighted by their sticking coefficients. Germanium growth dominates in the top half of the reactor while silicon growth dominates in the bottom regions.

with inlet gases (GeH_4, SiH_4) and ion-electron recombination. The electron temperature peaks at 3.5 eV adjacent to the antennae where power deposition is maximum and reduces to 2 eV away from the antennae as the result of the high inelastic collision frequency at 1 Torr and moderate electron thermal conductivity. The plasma potential peaks at 28 V and off-axis near the regions of high electron temperature where the ionization rate is also maximum. Similarly, the positive ion density also peaks off-axis at 9.4×10^{11} cm^{-3} where the plasma potential is most positive.

The densities of silicon and germanium growth species in the reactor are shown in figure 2. These densities are the sum of the densities of radicals multiplied by their sticking coefficient to map the potential for NP growth by germanium and silicon containing species. The density of GeH_4 is largest near the top inlet however the germanium growth density at that location is low due to the germane being directly non-reactive with NPs. The germanium growth density is highest in the vicinity of the first plasma zone where electron impact dissociation produces germanium radicals with non-zero sticking coefficients. As NPs sample different regions of the reactor, their growth varies in proportion to the growth densities of Ge and Si containing radical species.

The DTS tracks the instantaneous growth contribution from germanium and silicon as particles traverse the reactor. For the base plasma conditions, the evolution of particle growth contributions and transport at different stages of synthesis are shown in figure 3. Initially, the particles are electrostatically trapped in a disk-shape near the primary coil where germanium core growth dominates. This unique trapping structure is created by a balance between the axial and radial components of the forces. When the particles grow to a critical size (approximately 3 nm) the axial fluid drag force begins to dominate the force balance and push the particles down to the secondary plasma zone where shell growth occurs.

In the vicinity of the downstream shell growth zone, the particles are charged negatively and are trapped in a toroidal-shaped structure slightly above the second coil. The toroid of CSNPs is trapped for approximately 200 ms as the upward ion drag force balances the downward electrostatic and fluid drag forces. The core-to-shell growth transition begins at a reactor height of about 4 cm where the silicon growth contribution rises above 50%. Silicon growth contributions continue to increase downstream of the transition point due to the higher availability of smaller silane species (SiH_x, x=1−3), leading to rapid production of large silicon hydride radicals (Si_xH_{x+1}, x=1−12). The average fractional growth contributions of Ge and Si species along the trajectories of NPs as a function of reactor height are shown in figure 3(e) for the base case. Improvements in core and shell purity can be achieved by controlling the location at which the core–shell transition occurs. For example, an upward shift in reactor height of the core-to-shell growth transition point will yield CSNPs having purer cores and but possibly less pure shells.

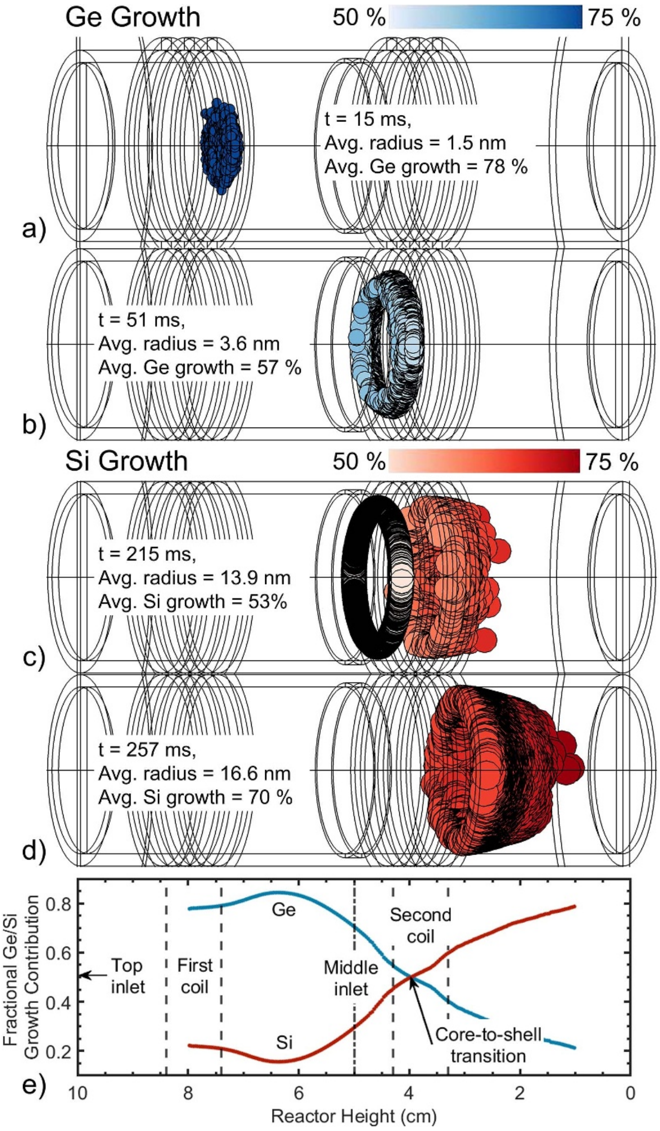

Figure 3. Snapshots of NP locations and germanium/silicon growth contribution at (a) 15 ms, (b) 51 ms, (c) 215 ms, and (d) 257 ms. The size of circles is scaled to particle size. The color indicates the degree of growth contribution by either (blue) germanium or (red) silicon. (e) The average growth contribution from germanium and silicon as a function of reactor height.

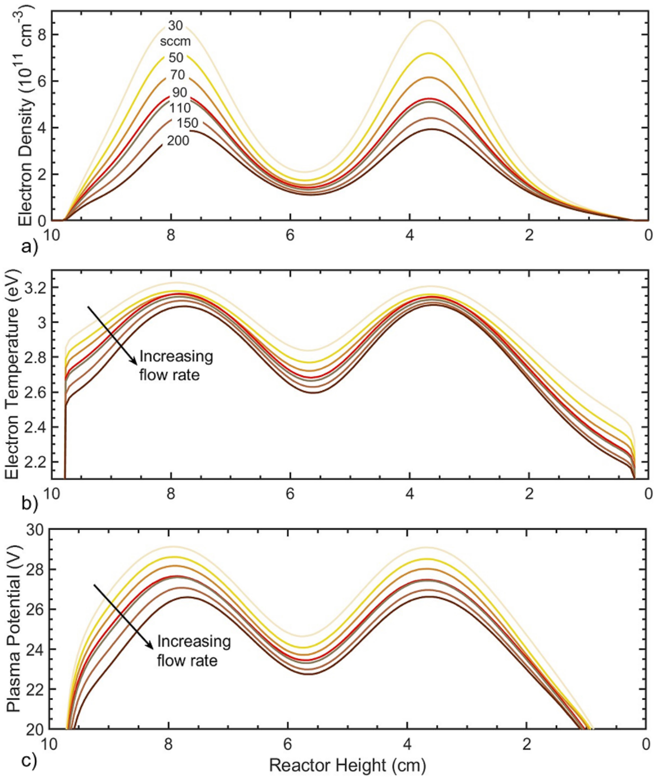

Figure 4. On-axis (a) electron densities (b) electron temperature and (c) plasma potential as flow rate of Ar/GeH$_4$ through the top nozzle is varied between 30 to 200 sccm.

The predicted NP properties are commensurate with those produced by Hunter *et al* [8] for Ge–Si CSNP, though operating conditions do differ. The predicted CSNP sizes are larger than observed by Hunter *et al* in their dual-plasma source reactor [28], a condition that is likely attributable to their shorter residence time.

3.2. Impact of gas flow rate

The primary mechanism for removing NPs from the electrostatic traps is the increase in viscous fluid drag force on the growing NPs. By varying the gas flow rate through the reactor, the average particle residence time both in the reactor and in traps can be controlled by the change in the resulting fluid drag force. NPs of all sizes experience a stronger downward acceleration by the increase in flow speed resulting from the increase in flow rate. However, relative to other forces, larger NPs are more sensitive to fluid drag.

To quantify the effect of fluid drag on NP properties, the gas flow rate supplied from the top inlet was varied from 30 to 200 sccm while maintaining 10 W of power deposition for both plasma zones. All other conditions were the same as for the base case. Since the applied power was kept constant, increasing inlet flow rate (reducing residence time) effectively reduces the energy deposition per molecule, which in turn influences the feed gas dissociation. The on-axis ($r = 0$) plasma properties for varying flow rates from the top nozzle as a function of reactor height are shown in figure 4. The lower energy deposition per molecule at higher flow rates produces less dissociation and lower rarefaction by gas heating with the end result being the power deposition per electron is larger. For constant power deposition, this leads to a lower on-axis electron density. The electron temperature increases with decreasing flow rate due to there being more diffusive transport that occurs at low flow rates while having more rarefaction. Electron loss through diffusion to the wall is higher and therefore a higher electron temperature is needed for a self-sustaining plasma. The plasma potential profile follows that of the electron temperature as plasma potential generally scales with electron temperature in a glow discharge.

Perhaps the most important impact on NP properties when varying operating parameters of the LTP reactor is the change to the particle trapping dynamics. Different modes of NP trapping occurred for low (<60 sccm), intermediate (65–85 sccm) and high (90–200 sccm) flow rates of Ar/GeH$_4$ from the top nozzle, as shown in figures 5–7. At low flow rates (figure 5), germanium cores were initially trapped on-axis where the axial electric field strength was large enough to balance the fluid drag force. When the NPs grew to a critical size (2.5–3 nm radius), the fluid drag force then dominated and flushed the NPs down to the secondary plasma zone for silicon shell growth. A ring-shaped structure formed near the secondary plasma zone. NPs in the ring negatively charge to higher values as the particles grow, resulting in an increase in the upward ion drag force. The balance between the axial ion drag and the electrostatic force enables the NPs to be trapped in the secondary plasma zone for a prolonged period (approximately 200 ms) before fluid drag de-traps the particles to flow out of the reactor.

There is a limit to flow control of NP properties. For example, if one attempts to synthesize CSNPs with larger cores or thicker shells by reducing the flow rate to increase residence time, loss of particles to the reactor wall will start to become an issue. Decreasing the flow rate below 30 sccm in the model led to more particle losses to the reactor wall which resulted in lower yield. The higher rate of wall collisions can be attributed to the higher radially outward ion drag force due to there being a larger ion flux at lower flow rates. This higher outward ion drag forces resulted in expansion of the toroidal trapping structure to the point of colliding with the reactor wall where, in our model, the NPs stick with unity probability. It is possible that NPs do not stick with unity probability or can be returned to the plasma through reactions with neutral or charged species. However, the return of NPs to the plasma after sticking to walls is not currently part of the DTS model.

In the intermediate flow rate regime (65–85 sccm), a core-growth dominated trapping mode with fractional splitting of CSNPs occurred. An example of this mode with 70 sccm flow from the top inlet is shown in figure 6. The NPs segregated into two traps in the primary zone plasma zone. The first batch of NPs are in a disk configuration about half the diameter of the tube at the lower edge of the coil set. The majority of the particles in the second batch, around 87%, were trapped in a toroidal configuration at the height of the coil set where the plasma potential is most positive. The splitting of particles into two traps occurred when NPs with different charge passed

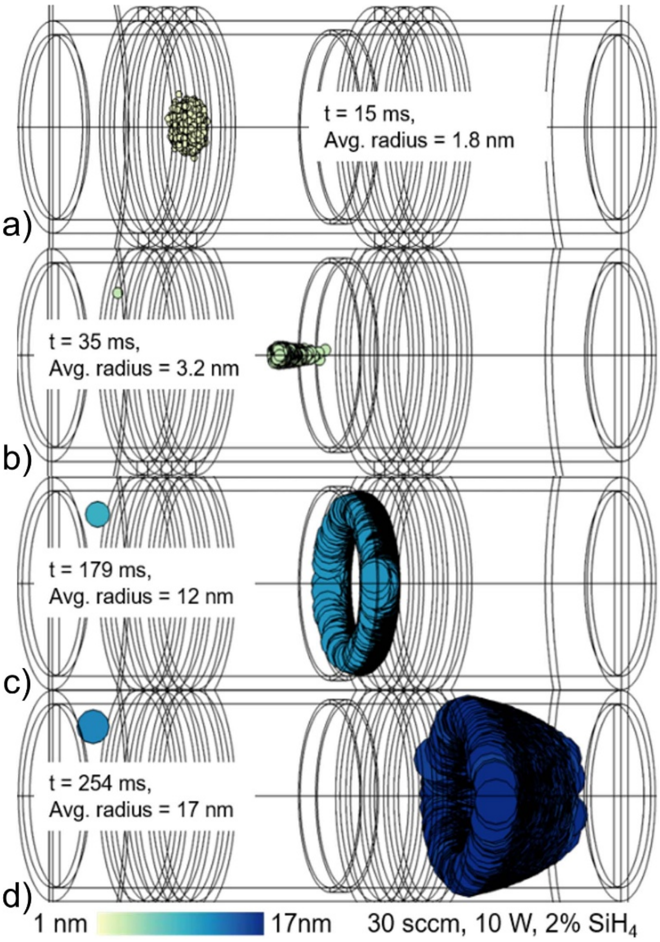

Figure 5. Snapshots of NP locations when a low top inlet gas flow rate (30 sccm) is used. The size of the particle is indicated by the size of the symbol and the color coding. The time and average NP radius are noted in each frame. (a) NPs are trapped at the primary plasma zone. (b) Fluid drag de-traps particles. (c) Large negative charge on the particles allow ion drag to trap particles in a ring structure in the secondary plasma zone. (d) Fluid drag de-traps particles from the second plasma zone.

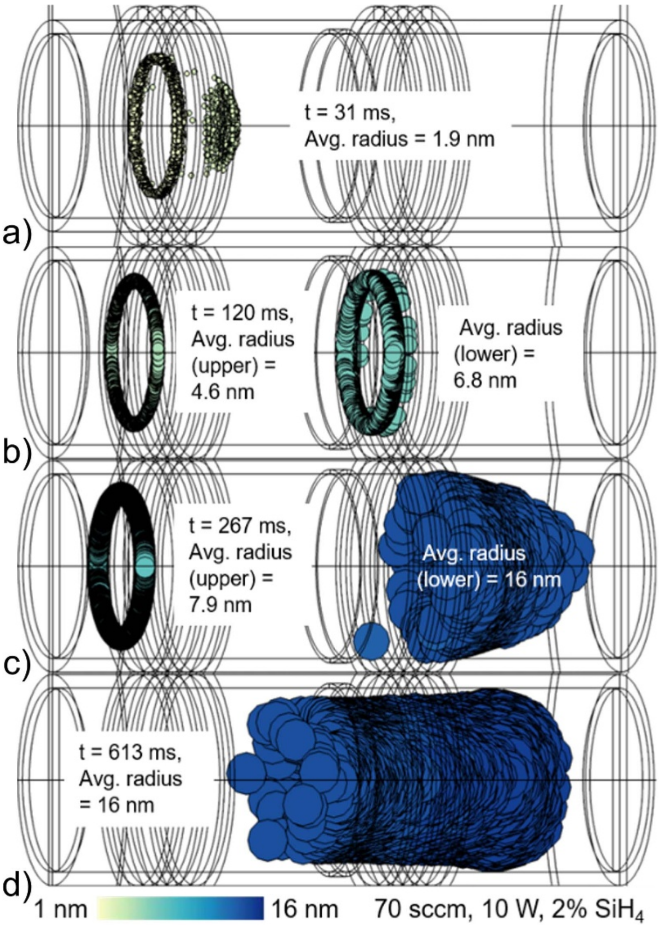

Figure 6. Snapshots of NP locations when an intermediate top inlet gas flow rate (70 sccm) is used. The size of the particle is indicated by the size of the symbol and the color coding. The time and average NP radius are noted in each frame. (a) NPs split into two batches at the primary zone, with the first batch being trapped lower and second batch being trapped higher in the plasma zone. (b) First batch flows to the secondary plasma zone and gets trapped. (c) First batch of NPs de-traps. (d) Second batch of NPs flows out of the reactor without further trapping at the secondary plasma zone.

through the center of the coil set. (Recall that the charging of the NPs at these small sizes is stochastic and statistical, so similarly sized particles may have different charge.) More negatively charged particles ($Q = -12q$) were accelerated upwards by electrostatic forces and entered a region of upward-pointing ion drag force (upper half of the first coil set). The more weakly charged NPs ($Q = -9q$) were trapped in the lower part of the coil set with downward-pointing ion drag as electrostatic forces failed to propel them into the upper region.

The first batch of NPs (lower trap) have a short residence time in the first plasma zone and so flow into the secondary plasma zone with a smaller core radius. These particles are trapped in the secondary plasma zone for about 150 ms, similar to the particle dynamics occurring in the low flow rate regime. The first batch of NPs flow out of the reactor sooner than the second batch, as shown in figure 6(c). Particles in the second batch (trapped higher in the first plasma zone) experienced tighter trapping due to their rapidly increasing negative charge, lengthening their residence time in the trap. With the longer residence time of NPs in the second batch, the particles grow to a larger size, producing a core of a larger radius. These large cores arrive at the secondary plasma zone and flow out of the reactor without any additional trapping, as shown in figure 6(d).

The particle dynamics at higher flow rates through the top inlet (90−200 sccm) are more stable and predictable, as shown in figure 7 for a flow rate of 150 sccm. Trapping of particles near the upper coil occurs in a single grouping due to the dominating axially downward fluid drag. After de-trapping (particle radius of 1.1 nm) from the primary plasma zone, NPs are trapped on axis near the secondary plasma zone. This trapping occurs for a shorter period of time (50 ms). The fluid drag force empties the trap with NPs exceeding 4.6 nm in radius. The NPs are tightly trapped on-axis due to the balance between the relatively constant (insensitive to flow rate variation) inward electrostatic force and the reduced radially outward ion drag and thermophoresis forces. Even with a slip boundary condition for fluid flow at the wall, at 1 Torr the flow

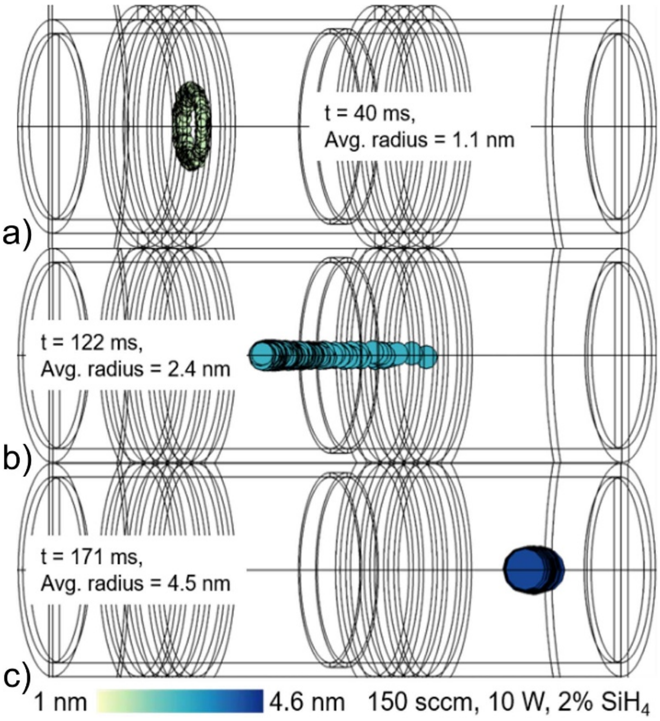

Figure 7. Snapshots of NP locations when a high inlet gas flow rate (150 sccm) is used. The size of the particle is indicated by the size of the symbol and the color coding. The time and average NP radius are noted in each frame. (a) NPs trapped near the primary plasma zone in ring structure. (b) Particles de-traps and flow downstream. (c) NPs trapped on-axis in the second coil region.

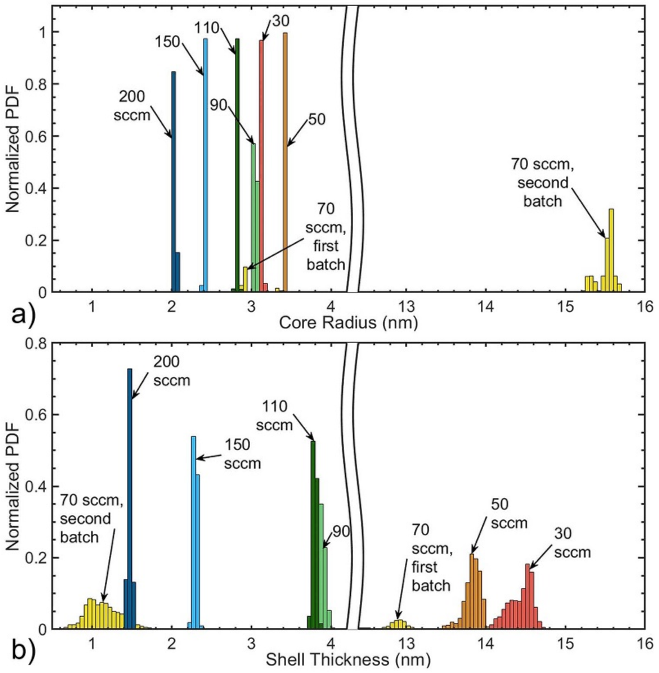

Figure 8. Normalized PDF of (a) core radius and (b) shell thickness when varying top inlet flow rate from 30 to 200 sccm.

speed (and so fluid drag) is largest on axis, which accelerates NPs more rapidly out of the trap than if the trapping were to occur off-axis (toroidal structure).

The normalized probability density functions (PDFs) of the core radius and shell thickness of CSNPs for different top inlet flow rates are shown in figure 8. At low flow rates (30–60 sccm), the core radius increases with increasing flow rate. The weaker radial ion drag force traps particles in a smaller ring in the vicinity of the first coil as flow rate increases. As the axial electric field strength peaks on-axis and is weaker at larger radius, NPs trapped near the center of the reactor (or in a narrower ring structure) experience a stronger upward electrostatic force which opposes fluid drag. As a result, the NPs are trapped longer and produce a larger core. The splitting of particles into multiple traps in for intermediate flow rate (65–80 sccm) produced a large fraction of CSNPs with large core radii (peaking at 15.5 nm when applying 70 sccm). In the high flow rate regime (90–200 sccm), the core radius decreases as the flow rate increases due to the larger fluid drag force which shortens trapping time in the Ge growth region. The range of core radii is not large, as the majority of the particles have cores of sub-4 nm and are less sensitive to viscous fluid drag forces. The change in the shell thickness when varying flow rates is more pronounced as the larger NP sizes in the secondary plasma zone are more sensitive to fluid drag forces.

A summary of CSNP properties is in figure 9. In general, as shown in figure 9(a), the shell thickness decreases as flow rate increases due to the reduced residence time in the second Si dominated plasma zone. The exception is when particles split into different groups in the primary Ge dominated plasma at intermediate flow rates. This is shown by the outlier case at 70 sccm. The radii of the Ge cores (3.1–3.4 nm) tend to be smaller than the Si shell thickness (13.7–14.3 nm) at lower flow rates (<60 sccm). At these flow rates, the Si shell growth is dominated by a longer trapping time (200 ms) in the lower plasma zone. Core radii and shell thickness are commensurate at higher flow rates (>90 sccm). With the exception of the outlier, CSNP morphology follows the trend of smaller particles having more equal core and shell dimensions with higher flowrate.

With concern that the 70 sccm case is an outlier, this intermediate flow regime was more finely investigated with the results shown in figure 9(b). First, the initial locations of particles (height and radius in the reactor) were varied and the same trapping behaviors occurred. When more finely varying flowrates, particle splitting into the two batches was nominal at 65 sccm, with only about 1% of the total number of particles being strongly trapped in the first plasma zone. At 70 sccm, particle trapping switched to core growth dominated mode. Approximately 87% of the NPs were trapped higher in the first plasma zone (second batch), producing CSNPs with large Ge cores and thin Si shells. Particle splitting into the two traps begins to lessen from 75 to 80 sccm. These results indicate that there are more stable and less stable operating regimes. The intermediate flow regime here is an unstable regime where small changes in process parameters, coupled with stochastic charging processes, produce chaotic-like outcomes. This variability is likely amplified by the finite number of particles used in the simulation, but is also likely a result of

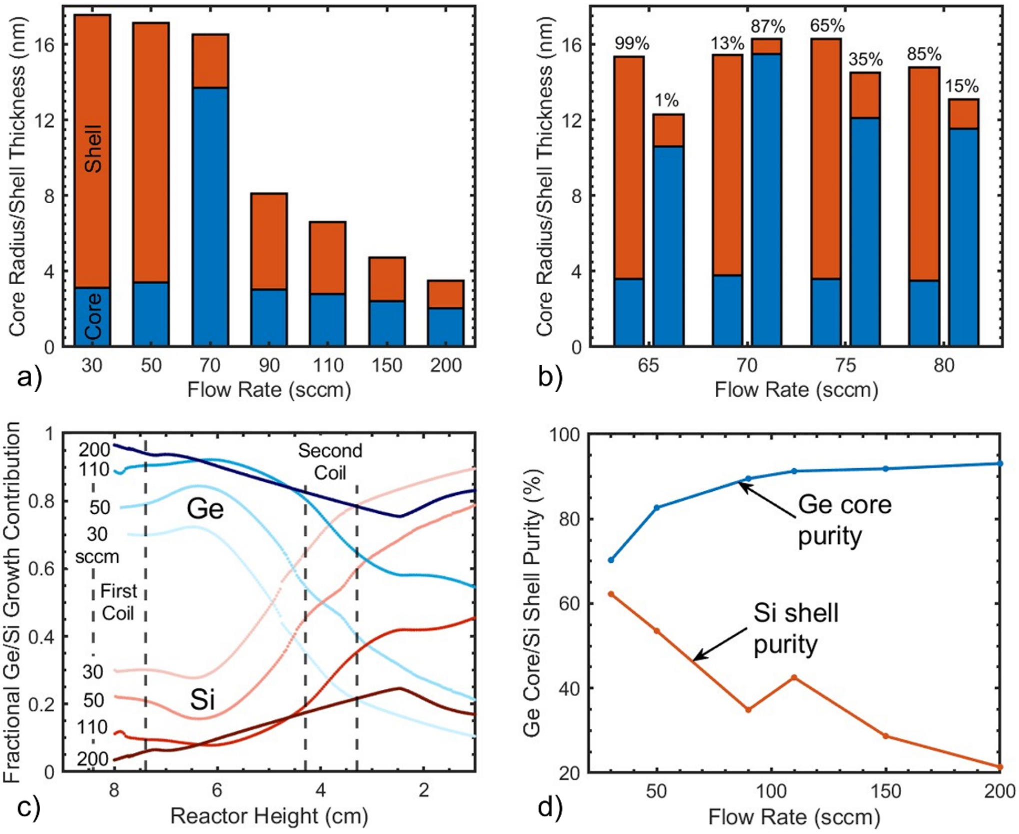

Figure 9. CNSP properties as a function of Ar/GeH$_4$ flow rate from the top inlet. (a) Average core radius and shell thickness. (b) Average core radius and shell thickness for intermediate flow rates (65–80 sccm). For each flow rate, the left column is for CSNPs in the first batch that is trapped lower in the first plasma zone (small core with thick shell), and the right column for the second batch that is trapped higher in the first plasma zone (large core with thin shell). The percentage of splitting between batches is indicated above each bar. (c) Average particle growth contribution from Si and Ge species along particle trajectories. (d) Core and shell purity.

operating near the boundary between two stable, but different, modes of operation.

The average fractional growth contributions along particle trajectories as a function of location of the NPs (reactor height) are shown in figure 9(c). Germanium growth dominates near the primary plasma zone and decreases downstream. Ar/GeH$_4$ flowing from the top inlet through the upper plasma zone locally produces Ge growth precursors whereas the Si growth precursors produced in the lower plasma zone must diffuse against the flow to the top of the reactor. As a result, Ge growth dominates. Silicon growth begins to dominate adjacent to the second plasma source due to the Ar/SiH$_4$ introduction from the middle inlet. There is not 100% utilization of the Ge growth precursors, and so minor Ge growth contributions continue downstream.

The core- and shell-purity as a function of flow rate are shown in figure 9(d). With an increase in top inlet flow rate, more germane (GeH$_4$) streams into the reactor and the axial fluid velocity increases, which suppresses silane (SiH$_4$) and silicon-growth precursors from back-diffusing into the upper plasma source. The core-to-shell transition point, the location where Ge and Si contributions intersect at 50%, transitions to lower in the reactor with increasing inlet flow rates. As a result of the higher proportion of Ge growth precursors in the upper portion of the reactor, the core purity increases with increasing flow rate (74% at 30 sccm to 95% at 200 sccm), while Si growth is less dominant in the secondary plasma zone. A core and shell transition does not occur for flow rates above 110 sccm. With a flow rate of 200 sccm Ge growth dominates throughout the entire reactor. This trends results, in part, from silicon species competing with the increasing flow of germanium species for power to dissociate into radicals in the secondary plasma zone at large flow rates.

With germanium-containing species dominating, their densities remain comparable across the flow rates. However, the silicon containing radical densities decreased from 5×10^{12} cm^{-3} at 30 sccm to 6×10^{11} cm^{-3} at 200 sccm. As a result, shell purity worsens when the GeH$_4$ inlet flow rate increases (62% at 30 sccm to 21% at 200 sccm). The decrease in Si purity at the intermediate flow rate (90 sccm) results from the NP trapping location being higher in the second plasma zone where Ge growth contributions are higher. In spite of the more predictable and stable particle trapping modes, shell purity is compromised at higher flow rates. One strategy to produce a purer shell would be lowering the germane fraction at the top inlet or increasing SiH$_4$ fraction at the middle inlet. The effect of SiH$_4$ fraction on CSNP properties is discussed in section 3.4.

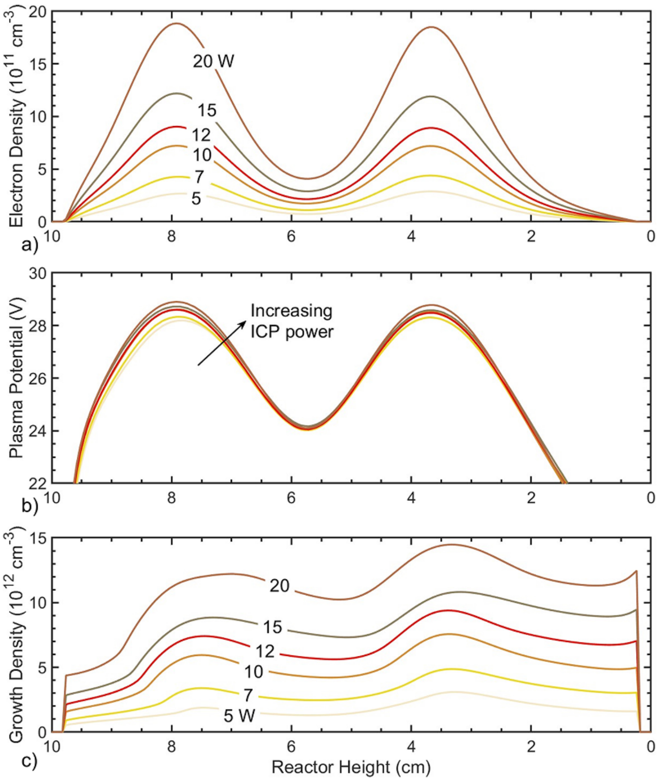

Figure 10. On-axis plasma properties as a function of height in the reactor for ICP powers of 5–20 W in each plasma zone. (a) Electron density, (b) plasma potential and (c) density of growth precursors.

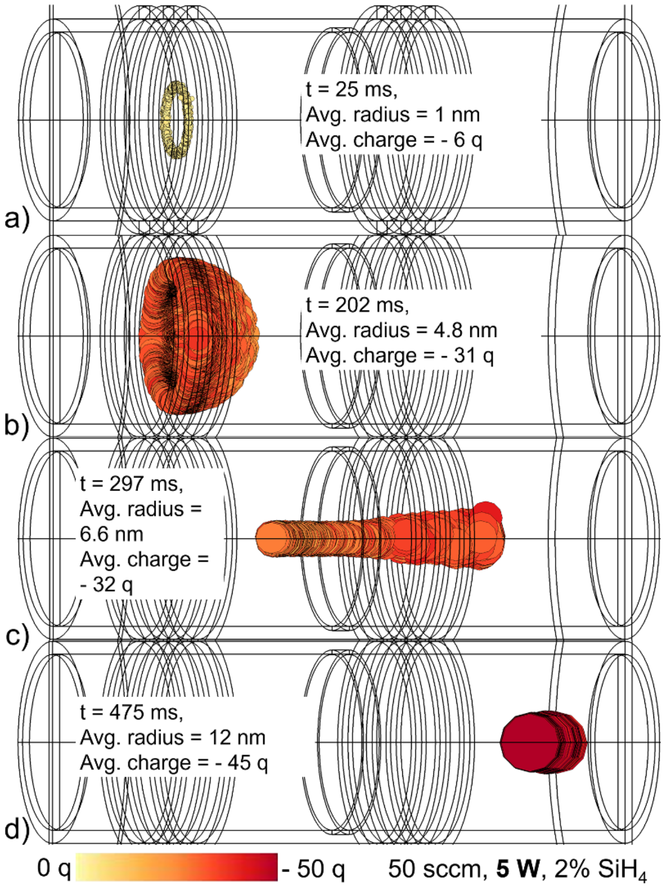

Figure 11. Snapshots of NP dynamics for 5 W of ICP power. The time, average radius and charge are noted in each image. The size of circles is scaled to the particle radius. The color gradient indicates the magnitude of charge on the particles. (a) Small particles are initially trapped in a ring and (b) form a 'bowl-like' structure as NPs grow larger. (c) NPs de-trap while (d) largely staying on-axis for shell growth downstream.

3.3. Impact of ICP power

NP transport in LTPs can be complex as the transport involves contributions from several forces with dynamically changing magnitudes with plasma properties, NP mass and charge. Charging of NPs plays a critical role in determining the trajectories of NPs and, to some extent, particle residence time, a factor directly related to growth. The impacts of ICP power on CSNP properties were investigated by varying the applied power in both plasma zones from 5 to 20 W while keeping the flow rates at Ar/GeH_4 = 98/2 at 50 sccm (top) and Ar/SiH_4 = 98/2 at 20 sccm (middle). The on-axis plasma properties as a function of power deposition and reactor height are shown in figure 10. As the power deposition increases, the plasma density increases as a result of increased rate of ionization from 1.3×10^{18} cm^{-3} s^{-1} at 5 W to 4.2×10^{19} cm^{-3} s^{-1} at 20 W. The plasma potential (and so depth of electrostatic traps) is a weak function of power, being nearly constant. A rise in the fractional dissociation of precursor gases GeH_4 and SiH_4 is reflected in the increase in growth species density with increasing power (3.1×10^{12} cm^{-3} at 5 W to 1.4×10^{13} cm^{-3} at 20 W) as shown in figure 10(c). The growth species density is the sum of the silicon and germanium containing radical densities scaled by their respective sticking coefficients.

The level of ICP power produces distinct particle transport dynamics in the reactor. Different trapping modes occurred at low (<5 W), intermediate (5.5–8.5 W) and high power (>9 W). The differences in the trapping modes are in part a consequence of the charging dynamics of the NPs. Particles dynamics are shown in figure 11 for an ICP power of 5 W. Particles are initially trapped in a ring structure in the upper plasma zone. As NPs grow in size, they accumulate charges ($-6q$ at 1 nm to $-31q$ at 4.8 nm) and experience strengthened electrostatic traps, as shown in figures 11(a) and (b). After approximately 200 ms of core growth, a bowl-shaped structure emerges (figure 11(b)) with heavier and weakly charged particles being trapped further downstream at the bottom of the bowl due to the greater fluid drag force and weaker electrostatic forces on axis. The contour of the bowl traces out the locations where the electrostatic forces balance the ion drag force for NPs of a given size and charge. Once the particles have grown to a critical size (>6.5 nm) fluid drag dominates and NPs flow to the second coil.

The particles are mostly trapped on axis near the second coil due to the stronger radial electrostatic force compared to ion drag force that accelerates negatively charged NPs towards the axis. Particles grow (6.6 nm to 12 nm) and charge more negatively ($-32q$ to $-45q$) as they cross the second coil region on axis. For a few hundred milliseconds, these negatively charged NPs are trapped a few centimeters above the outlet where the

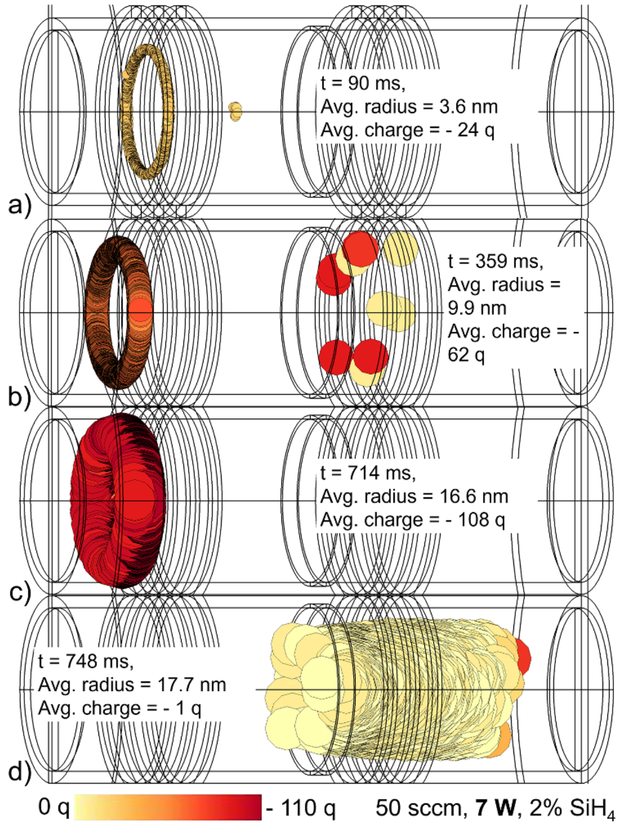

Figure 12. Snapshots of NP dynamics for 7 W of ICP power. The time, average radius and charge are noted in each image. The size of circles is scaled to the particle radius. The color gradient indicates the magnitude of charge on the particles. (a) Particles trap in a ring during core growth with minor splitting occurring. The first batch of NPs is trapped lower and second batch is trapped higher in the first plasma zone. (b) Particles in the first batch detrap to the secondary plasma zone. (c) Strong trapping force enables longer trapping in the primary zone. (d) Particles flow downstream without trapping at the secondary coil.

upward pointing electric field is the strongest (figure 11(d)). The NPs reside in this trap until pulled out of the trap by fluid drag.

With an intermediate power (7 W, figure 12), particle splitting into two batches occurred in a similar fashion as observed at intermediate flow rates. The majority of the NPs are trapped in a ring structure in the upper region of the primary plasma zone for a prolonged period (700 ms). The NPs grow (0.5 nm–16.6 nm) while collecting charge ($-1q$ to $-108q$), which results in the electrostatic trap strengthening due to the increasing ion drag force. Eventually, the fluid drag force dominates and particles flow downstream to the shell synthesis zone. Due to the large Ge core that has been produced in the top plasma zone and the middle inlet introducing more flow, there is little trapping of particles near the secondary plasma zone as the fluid drag force dominates. Statistically, a few particles charge in such a manner that they are trapped lower in the first plasma zone, causing them to detrap sooner than the particles in the ring structure. These statistical outliers contribute to non-monodisperse distribution of NP properties.

The NPs that assemble in a ring adjacent to the lower antenna near the wall have little charge whereas the particles in the ring away from the lower antenna are highly negatively charged. Near the reactor wall, the electron temperature is lower and negative ion density is higher. The electronegativity (negative ion density compared to electron density) is 0.2 on axis (negative ion density 1.1×10^{11} cm^{-3}) and 1.5 off axis (negative ion density 2.5×10^{11} cm^{-3}). These conditions result in a lower negative charge on NPs as they pass through the secondary plasma zone.

At high ICP powers (>9 W) the modes of particle trapping stabilize in a manner similar to those at high flow rates. NP properties are shown in figure 13 for ICP power of 15 W. Ge core growth occurs in the primary plasma zone where NPs are trapped until fluid drag forces dominate and de-trap the NPs. The NPs are then trapped in a ring 0.5 cm above the secondary antenna where shell growth occurs and the particle charge increases. Particle growth occurs quickly as the total density of growth species increases with power deposition. After less than 100 ms, the particles achieve a critical size (9 nm) and flow down to the secondary zone in a broad toroidal structure. The larger, more highly charged particles are more susceptible to thermophoretic and ion drag forces and the trapping location expands to a larger radius in the reactor. Particles lose their charge when emerging from the second plasma zone and little to no trapping occurs downstream. The widening of the ring shaped trapping structure at higher power results from the increasing radially outward ion drag force. This widening of the trap also increases losses to the walls and so is detrimental to CSNP yield. Approximately 10% of NPs are lost to the walls at 15 W and 90% are lost at 20 W of ICP power. Nearly all particles (99.8%) are lost at 25 W.

The distributions of the core radius and shell thickness are shown in figure 14 for ICP powers of 5 W to 20 W. NPs are trapped near the bottom of the primary plasma zone during Ge core growth due to the increasing downward ion drag force. As a result, the core tends to be smaller at larger applied power (2.8 nm at 15 W and 6.2 nm at 5 W). An exception occurs for the intermediate power (7 W) where NPs are trapped in the upper portion of the primary plasma zone where the ion flux and ion drag force are pointed upwards. The core radii across all ICP powers tend to be mono-disperse, indicating an abrupt transition from NPs being trapped and being de-trapped.

Generally, the thickness of the shell follows a similar trend of decreasing thickness with increasing power. Larger core radii tend to correlate with thinner shell thickness. The ion drag forces are larger at higher ICP power, which combined with the increased fluid drag forces acting on the larger core particles, reduce the residence time of those NPs in the Si-dominated lower plasma zone. This reduced residence time results in thinner shells. The thicknesses of the shells are less monodisperse than the cores, a consequence of more variability in trapping times and trajectories of NPs in the lower plasma zone.

The final particle dimensions (core radius and shell thickness) as a function of ICP power are shown in figure 15(a).

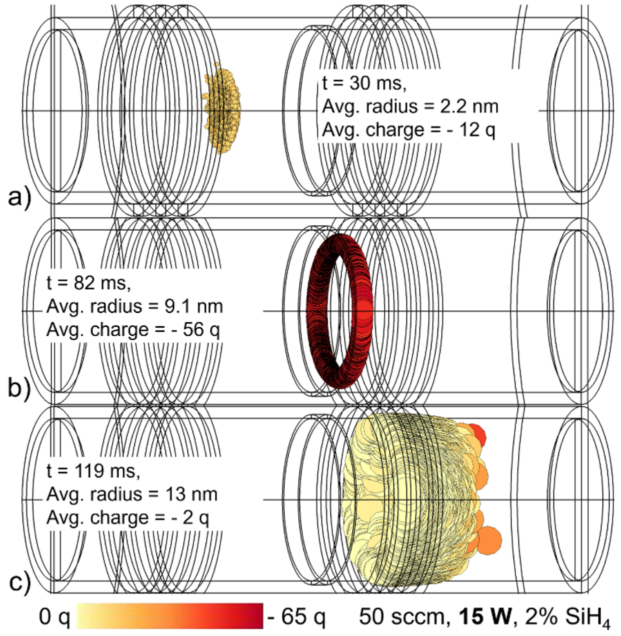

Figure 13. Snapshots of NP dynamics for 15 W of ICP power. The time, average radius and charge are noted in each image. The size of circles is scaled to the particle radius. The color gradient indicates the magnitude of charge on the particles. (a) Particles are trapped in a disk during core growth. (b) Particles are trapped in the second plasma zone. (c) De-trapping occurs and particle assemble into a wide ring.

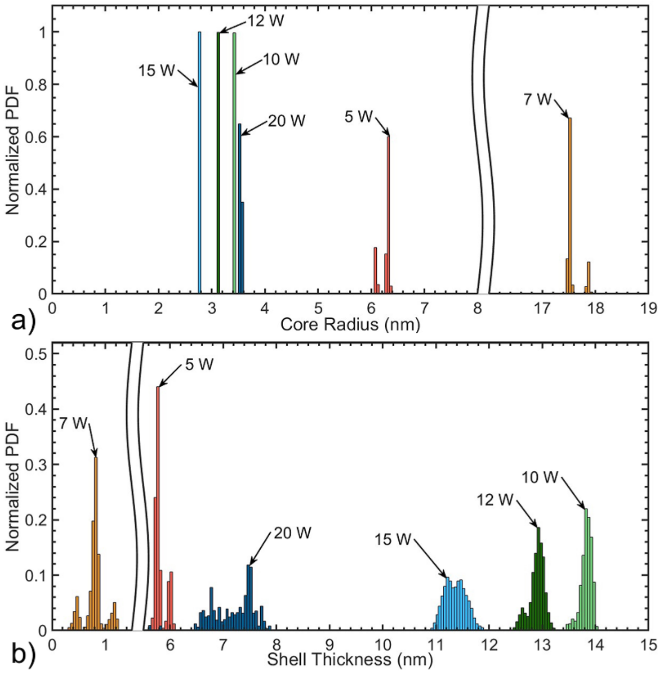

Figure 14. Normalized particle distribution functions (PDFs) of (a) core radius and (b) shell thickness when varying ICP power in each source from 5 to 20 W.

At low ICP power, the particle sizes tend to be smaller as the trapping locations are generally on-axis. With the pressure being high enough that there is little slip at the walls, the fluid velocity is maximum on axis. The higher speed then more rapidly de-traps particles on axis, shortening their residence time for growth. For intermediate ICP power, the combination of higher radical density and longer trapping time increased the core radius by more than a factor of 2 and increased the overall particle size. However the larger particle is more susceptible to fluid drag, which lowers residence time in the lower plasma zone, producing a thinner shell. At high ICP powers (10–20 W), NP radius decreases with increasing power as a consequence of the shorter trapping times of NPs in larger diameter toroids, which in turn decreased particle residence time and promoted particle losses to the walls.

CSNPs produced with the intermediate ICP power of 7 W tend to split into two separate batches due to statistical variation in charging and force dynamics, as shown in figure 12. The trapping behavior of the first batch of NPs is shell growth dominated, similar to the trapping observed with low and high ICP power. Trapping occurs momentarily (tens of ms) near the bottom half of the first plasma zone before the particles flow down to the secondary plasma zone where they are trapped for longer duration (hundreds of ms), producing CSNPs with small cores and thick shells. The second batch of particles initially move to the top half of the first plasma zone as they are highly charged. These particles are trapped for hundreds of ms by the upward ion drag force. Once these NPs achieve a large critical size (17–19 nm), they flow down to the secondary plasma zone where little to no trapping occurs. The second batch of CSNPs have much larger cores and thinner shells when compared to the first batch, and they are usually larger in overall size as they reside in the reactor for a longer period of time. Simulations were performed for finer gradations in power in the vicinity of 7 W and the results are shown in figure 15(b). The core growth dominated trapping mode persists throughout the range from 6 W to 8 W. The percentage split between the first and second batches of CSNPs changes for different ICP powers. The trapping slowly transitions to a stable shell growth dominated mode below 6 W and above 8 W as the particles splitting becomes less significant (0.1%–4% NPs in stable shell growth dominated trapping mode).

The impact of varying ICP power on the core and shell purity is shown in figures 15(c) and (d). Dissociation of inlet gas to produce Ge containing growth radicals increases with increasing ICP power while back diffusion of Si containing species decreases due to gas heating. Consequently, the germanium growth contribution near in the primary plasma zone increases as power increases while that from Si decreases. The transition between Ge and Si dominated growth occurs at nearly the same location in the reactor as a function of power. Since the flow rates and inlet gas fractions are constant, the densities of Ge and Si growth species scale similarly with power. However, since the top inlet flow rate of Ar/GeH_4 is two and a half times that of the middle inlet flow of Ar/SiH_4, there is a disproportionate increase in Ge precursor flowing downstream with increasing power, which decreases Si shell purity.

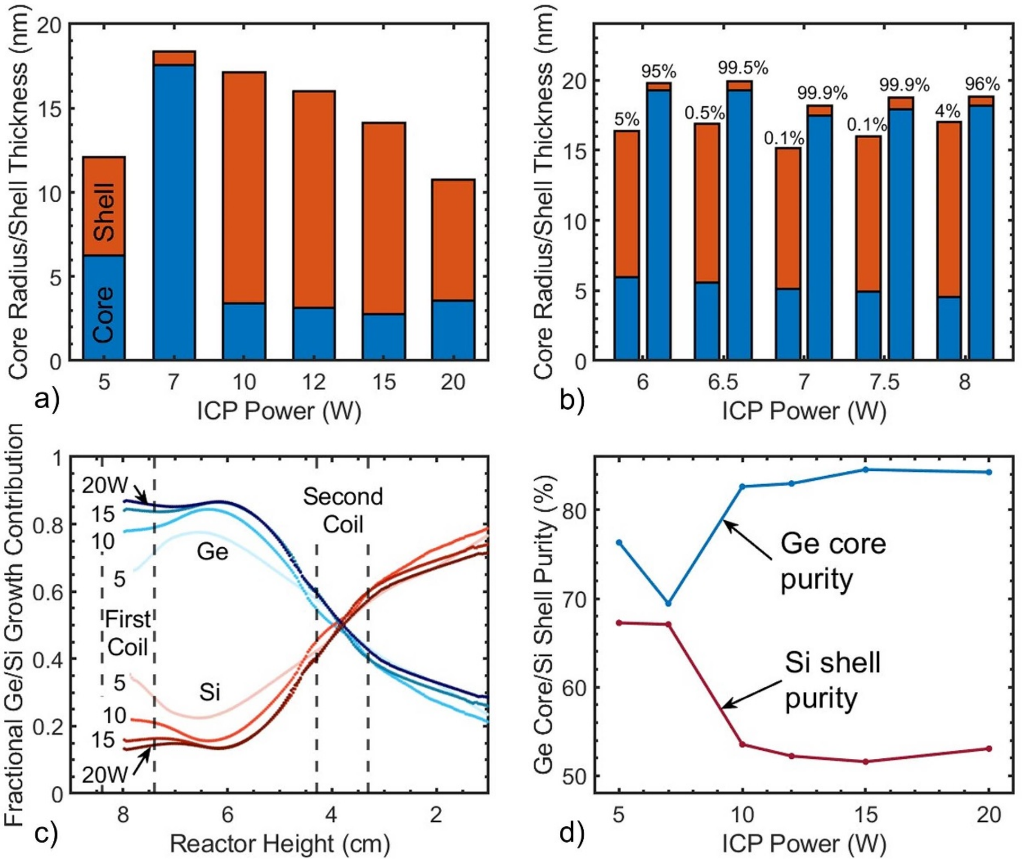

Figure 15. CNSP properties as a function of ICP power. (a) Average core radius and shell thickness. (b) Average core radius and shell thickness for intermediate power (6–8 W). The left column is for CSNPs in the first batch trapped primarily in the secondary plasma zone (small core with thick shell), and the right column for the second batch trapped primarily at the first plasma zone. (Large core with thin shell). The split percentage is indicated above each bar. (c) Average particle growth contribution from Si and Ge species along particle trajectories. (d) Core and shell purity.

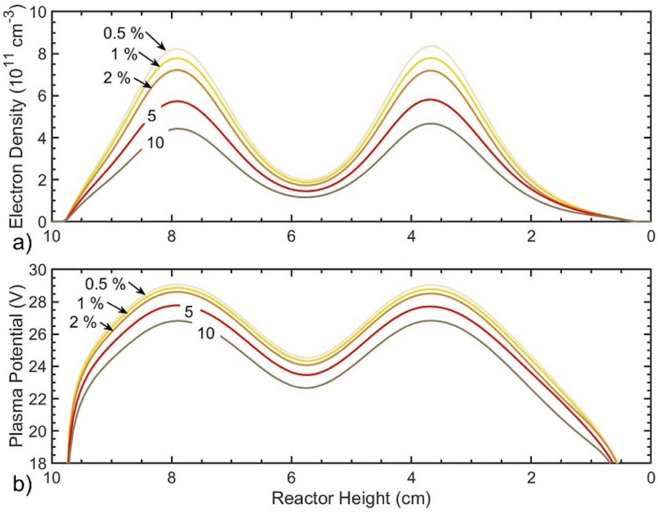

Figure 16. On-axis plasma properties as a function of height in the reactor for inlet silane fractions of 0.5% to 10%. (a) Electron density and (b) plasma potential.

3.4. Impact of inlet silane fraction

The impact of varying Ar/SiH$_4$ gas composition flowing into the reactor from the middle inlet was investigated. The inlet flow mole fractions were varied from Ar/SiH$_4$ = 99.5/0.5 to Ar/SiH$_4$ = 90/10 while keeping the ICP power (10 W in each source) and flow rates constant (50 sccm top and 20 sccm middle). The on-axis plasma properties when varying silane fraction are shown in figure 16. An increase in silane flow rate increases the non-ionizing power loss by electrons dissociating silane into radicals for particle growth. With these non-ionizing processes leading to electron power losses that otherwise could be utilized for ionization, the electron density decreases with the increase in silane inlet fraction. The electron density decreases from 8×10^{11} cm^{-3} at Ar/SiH$_4$ = 99.5/0.5 to 4.2×10^{11} cm^{-3} at Ar/SiH$_4$ = 90/10. The magnitudes of the change in electron density in the primary and secondary plasma zones are similar (though higher for the secondary plasma zone), which indicates the backflow of silane upstream is not negligible. Introducing more silane also allows for larger rates of formation of negative ions (SiH$_x^-$). The on-axis plasma potential peaks with smaller values for higher silane fractions, as shown in figure 16(b), which reflects the lower electron temperature and higher electronegativity.

The NP trapping dynamics for low silane fractions (0.5%–2%) are stable without there being splitting or strengthened trapping in the primary plasma zone, as shown

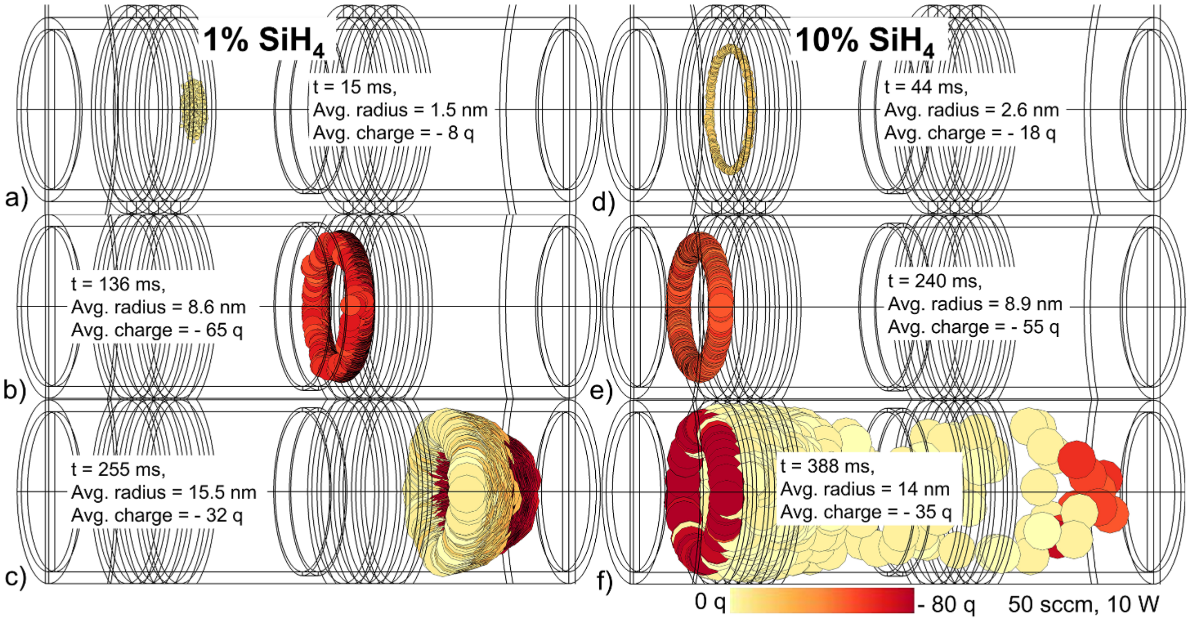

Figure 17. Snapshots of NP dynamics for (a)–(c) 1% and (d)–(f) 10% SiH$_4$ inlet fraction. The time, average radius and charge are noted in each image. The size of circles is scaled to the particle radius. The color gradient indicates the magnitude of charge on the particles. Particle trapping mode switches from shell- to core-dominated growth when the SiH$_4$ inlet fraction was increased from 1% to 10%.

in figures 17(a)–(c). For 1% SiH$_4$, NPs initially form a toroidal structure in the upper plasma zone, growing to a critical radius of 2.8 nm before flowing downstream. Particles then are trapped in a wide torus 0.5 cm above the secondary coil for about 230 ms. The wide toroidal structures formed with high ICP powers and low flow rates led to particle losses to the wall and reduced CSNP yield. However, few particles are lost to the walls at low silane fractions even when the torus is the widest. At low silane fractions, the radial thermophoretic force is weaker as a result of reduced gas heating in the secondary plasma zone, which then reduces the forces driving particle collisions with the wall.

When increasing silane inlet fraction to above 5%, the particle trapping mode shifts to be more core-growth dominated, similar to particle dynamics at intermediate flow rates and power (figures 6 and 12). At 10% inlet silane fraction (figures 17(d)–(f)), the large average negative charge ($-18q$) on the particles resulted in electrostatic force accelerating the particles to the upper half of the primary plasma zone, as shown in figure 17(d). The trapping then proceeds to occur a few cm above the top coil set where ion drag force is pointing upwards. The increase in the upward ion drag force, combined with the smaller off-axis fluid drag, traps the particles for a prolonged time (approximately 380 ms) in the primary plasma zone for core growth. Fluid drag eventually de-traps these large Ge cores towards the shell growth region. However, these particles experience no further trapping due to their large size (17.6 nm) and flow out of the reactor.

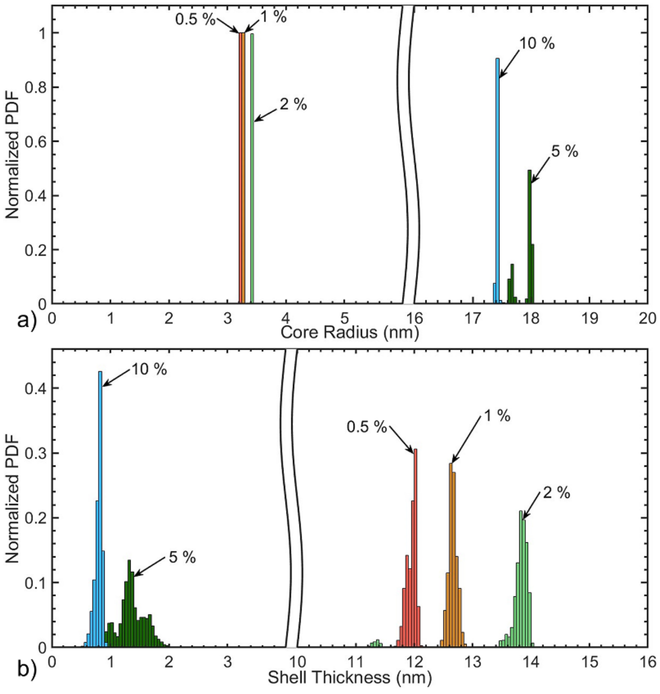

Figure 18. Normalized particle distribution functions (PDFs) for (a) core radius and (b) shell thickness when varying silane inlet fraction from 0.5% to 10%. As inlet fraction increases from 0.5%–2%, core and shell dimensions increase. Between 5 and 10% inlet fraction, core and shell dimensions decrease.

The core and shell size particle distribution functions (PDFs) as a function of silane inlet fraction are shown in figure 18. For lower inlet silane fractions (0.5%–2%), the Ge core radius is nearly constant (3–3.5 nm radius). NPs are trapped near the bottom of the primary plasma zone during core growth. Since the electric field strength and electrostatic force near the primary antenna are similar at low silane fractions, there is little change in the trapping time. At higher silane fractions (5%–10%), large cores were produced as the particles were trapped near the top half of the first coil set where the axial ion drag force points upwards.

Shell growth in the secondary plasma zone strongly depends on the charge of the NPs and their trapping locations. For silane fractions of 0.5%, 1% and 2%, the maximum charge of particles trapped in the secondary plasma were $-83q$, $-89q$ and $-94q$. A larger average charge produced a stronger electrostatic trap and longer particle residence time in the shell growth region. The increase in NP growth rate with increasing silane fraction, combined with the stronger electrostatic trapping, results in the CSNP shell thickness increasing from 11.9 nm to 13.7 nm for silane fractions of 0.5%–2%. At larger silane fractions (5%–10%), CSNPs were produced having thin shells (1.4 nm at 5% and 0.9 nm at 10%). With large core sizes, fluid drag forces sweep the particles through the secondary plasma zone without trapping reducing residence time in the shell growth zone.

The general trend of increasing CSNP size with increasing inlet silane fraction is shown in figure 19(a). The radius of the core increased between 2% and 5% silane fraction due to the a transition to strong trapping in the primary core growth zone. At 10% silane fraction, the higher growth rate afforded by the higher silane fraction could not compensate for the reduction in particle residence time in the secondary plasma zone, which further thinned the shell.

The average fractional growth contribution from silicon and germanium species, and resulting core/shell purity are shown in figures 19(b) and (c) when varying silane inlet fraction from 0.5% to 10%. Increasing silane fraction flowing from the middle inlet led to a higher density of silicon radicals in the secondary plasma zone (2.2×10^{12} cm^{-3} for 0.5% SiH$_4$ to 5.8×10^{12} cm^{-3} at 10%). This higher density of silane radicals, and their diffusion upstream, resulted in the core-to-shell growth transition point shifting upwards in the reactor. The increasing flux of silane radicals resulted in a decrease of 38% in Ge core purity while enabling a nearly equal increase (34%) in shell purity. The increase in shell purity and decrease in core purity saturates above a silane fraction of 5%. At this point, the silane radical production is limited by the power deposition.

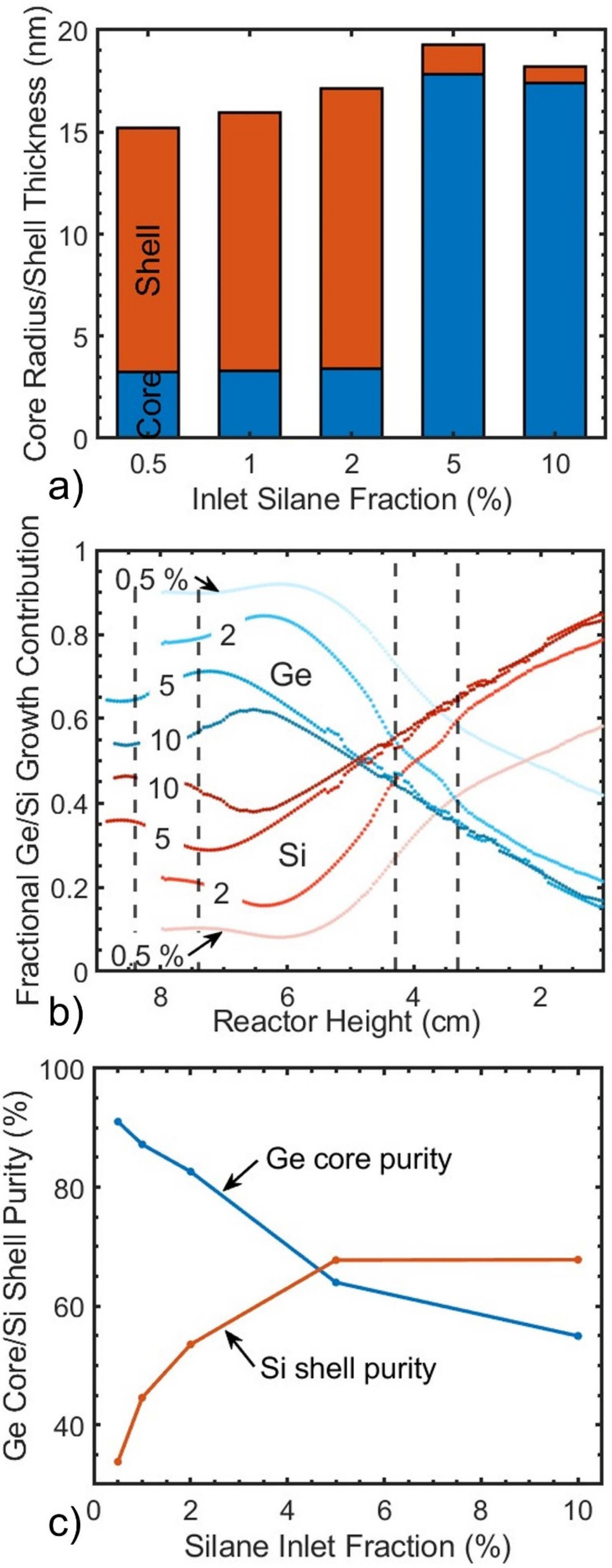

Figure 19. CNSP properties a function of silane inlet fraction. (a) Average core radius and shell thickness. (b) Average particle growth contribution from Si and Ge species along particle trajectories. (c) Core and shell purity.

4. Concluding remarks

The synthesis of Ge core and Si NPs (CSNPs) in a two-zone cylindrical ICP reactor was computationally investigated through dynamic tracking of particle growth, charging and their transport. Ar/GeH4 was injected through the top of the reactor with the primary (upper) ICP intended for Ge core growth. With Ar/SiH$_4$ introduced at the center of the reactor, the secondary (lower) ICP zone served primarily for shell growth. The plasma dynamics (ion fluxes, electron temperature, gas heating, plasma potential) in each plasma zone provide opportunities for trapping that contribute to synthesizing larger radii cores and thicker shells. That said, the growth of the core and shell are not independent. De-trapping of particles typically results from fluid drag on larger particles. A large core particle produced in the upper plasma zone that is de-trapped and entrained in the gas flow may then have a shorter residence time in the lower plasma zone, producing a thinner shell. The forces acting on NPs (electrostatic, ion drag, fluid drag, thermophoretic, gravitational, and interparticle Coulombic force) dynamically change with changes in reactor conditions and uniquely depend on particle size. Varying gas flow rate, ICP power and inlet silane fractions resulted in individual forces increasing (or decreasing) which combined with their dependence on size of the NP resulted in NP properties (core size, shell thickness, core/shell purity) being sensitive to small changes in operating conditions. While it is most often the case that fluid drag is the major force behind the removal of CSNPs from the reactor as they grow, flow rate is not the only the particle dynamic that determines residence time. For example, a slightly steeper temperature gradient (perhaps through changing ICP power) and larger thermophoretic force can translate a particle into a region of the reactor where the particle charge will increase, which in turn increases the ion drag and electrostatic forces acting on it, creating a cascading effect on the evolution of particle trajectory.

Two primary trapping modes were observed—core- and shell-dominated growth modes. In the core-dominated growth mode, particles are initially trapped in the upper portion of the primary ICP zone for an extended period. The axially upward ion drag force creates strong traps that produced CSNPs with large cores and poly-dispersed thin shells. Shell-dominated growth mode occurs when particles quickly de-trap from the upper plasma zone and are subsequently trapped in the secondary plasma zone where thicker shells are produced. Apart from these two modes, particles also split into batches (accumulation in sub-traps) with some particles de-trapping earlier than the others. These spatially diverse traps result in non-uniform size distributions of cores and shells and what appears to be chaotic behavior. The source of the chaotic behavior appears to be stochastic charging of the particles that will transport particles into different regions of the reactor characterized by unique trapping dynamics. Loss of CSNPs to the walls of the reactor typically occur when ion drag and thermophoretic forces broaden toroidal traps to the point that particles are pushed into the walls.

When varying gas flow rate, stable and unstable growth regimes occurred. Generally, increasing gas flow rate reduces particle residence time in the reactor due to increasing fluid drag force, resulting in smaller CSNP size, with shells thinning more rapidly than the core radii decrease. At intermediate flow rates stochastic particle dynamics produced spatially distinct trapping zones, which produced chaotic particle properties. Core purity improves with higher flow rate that diminishes back diffusion of silane radicals into the upper plasma zone while shell purity worsened due to greater mixing of germane and silane gas in the secondary plasma zone. ICP power impacts the dissociation fraction of precursor gases and plasma density, which in turn produces different charging environments at varying ICP power levels. A trend of decreasing CSNP size with increasing ICP power is partly attributable to less charging of particles in the periphery of the reactor. Core purity improves with increasing power but the shell purity decreases simply due to the higher availability of Ge precursors.

Varying SiH_4 fraction at the middle inlet directly impacts the growth species density near in the shell synthesis zone. A stable, shell-dominated trapping mode occurred at low SiH_4 fractions. Transition into core-growth dominated trapping occurs at larger SiH_4 fractions as the cores were charged more negatively and trapped for longer periods. Increasing SiH_4 fraction through the middle inlet resulted in less pure cores but improved shell purity. At high SiH_4 fractions, the core and shell purity plateau as the ICP power, instead of precursor availability, begins to limit growth.

From the parametric studies discussed here, there are tradeoffs that likely need to be made when tuning parameters (e.g. flow rate, power) with the end goal being to synthesize CSNPs of a certain dimension or purity. Often, the optimized parameters to produce CSNPs of a certain size come at the expense of the CSNP purity, or vice versa. If the goal is to control the core and shell dimensions, controlling the inlet flow rates can produce predictable results without significant compromise on core and shell purity. Among the three parameters investigated here, tuning the inlet silane fraction had significant impact on the purity of the core and shell components while having a weak effect on the CSNP component dimensions. This discussion of control of CSNP properties was based on a fixed reactor configuration. However, other reactor designs could be tailored toward synthesizing CSNPs of a certain specification. For example, utilizing a lower flow rate at the top inlet in combination with a larger diameter cylindrical tube for the secondary plasma zone would likely produce CSNPs with both large Ge core and thicker Si shell.

The intent of this investigation was to demonstrate and emphasize the complex dependencies of plasma operating parameters on particle trapping, core radii, shell thickness, and purity of core and shell during CSNP synthesis. Dual ICP plasma sources were chosen for this demonstration as their properties are more spatially confined and separately controllable compared to the CCP sources that are more often used. The higher plasma densities of ICP sources compared to CCPs can be problematic to the yield of metal or conductor NPs with relatively low melting points [43]. With ICPs typically having larger ion-to-radical ratios, formation of metal and conductor NPs can be suppressed in ICPs as a result of heating dominantly from ion-recombination and surface reactions with radicals [29]. Due to the plasma potential, gas heating and location of ion production in CCPs being more complex than ICPs, control of the CSNP growth dynamics will also be more difficult in CCPs. Regions of electrostatic trapping in CCPs are less well-defined than in ICPs due to the ionization source being more spatially uniform, which may introduce uncertainties in NP transport dynamics.

That being said, CCPs have been successful and efficient in synthesizing NPs for wide range of materials due, in part, to their lower plasma densities and less intense heating compared to ICPs [43–47]. While the results discussed here are for an ICP reactor, we expect similar trends in CSNP properties when varying the parameters discussed here in CCP reactors. The caveat may be that the transition between growth regimes would likely be less abrupt in CCPs due to the plasma being less confined. Since the spatial distribution of neutral growth species is less sensitive to ICP or CCP plasma generation, the trend for purity of the core and shell components predicted for ICPs can be comparable to that of CCPs. CSNP dimensions that result from transitions between trapping locations are likely to have the most variability between ICPs and CCPs.

To take advantage of the potentially finer control of CSNP synthesis afforded by ICPs, excessive particle heating must be avoided. Strategies to achieve this goal include low power ICPs that would avoid capacitive coupling (that is, avoid operating in the E-mode), pulsed ICPs to lower the average heating rates of particles, operating with buffer gases with lower atomic (or molecular) mass to increase heat transfer from the particles to cooler gas, or lowering the average ionization potential of the gas to lower the ion-induced heating of the particles.

Data availability statement

The data that support the findings of this study are contained in the paper (and supplementary files) and available from the corresponding author upon reasonable request.

Acknowledgment

The authors thank Professor Uwe Kortshagen for his insights on the topic of this paper. This work was supported by Army Research Office MURI Grant (W911NF-18-1-0240) and the Department of Energy Office of Fusion Energy Science (No. DE-SC0020232).

Conflict of interest

The authors have no conflicts of interest to disclose.

ORCID iDs

Yifan Gui https://orcid.org/0000-0003-0255-0308
Eve Lanham https://orcid.org/0000-0001-9715-4134
Mark J Kushner https://orcid.org/0000-0001-7437-8573

References

[1] Ghosh Chaudhuri R and Paria S 2012 *Chem. Rev.* **112** 2373
[2] Wei S, Wang Q, Zhu J, Sun L, Lin H and Guo Z 2011 *Nanoscale* **3** 4474
[3] Schärtl W 2010 *Nanoscale* **2** 829
[4] Mélinon P, Begin-Colin S, Duvail J L, Gauffre F, Boime N H, Ledoux G, Plain J, Reiss P, Silly F and Warot-Fonrose B 2014 *Phys. Rep.* **543** 163
[5] Reiss P, Protière M and Li L 2009 *Small* **5** 154
[6] Rai P, Majhi S M, Yu Y T and Lee J H 2015 *RSC Adv.* **5** 76229
[7] Lei Y and Chim W K 2005 *J. Am. Chem. Soc.* **127** 1487
[8] Hunter K I, Held J T, Mkhoyan K A and Kortshagen U R 2017 *ACS Appl. Mater. Interfaces* **9** 8263
[9] Chatterjee K, Sarkar S, Jagajjanani Rao K and Paria S 2014 *Adv. Colloid Interface Sci.* **209** 8–39
[10] Shaktawat S, Singh K R, Thapa S, Verma R, Singh J and Singh R P 2023 *Mater. Lett.* X **17** 100187
[11] Tsuji R *et al* 2008 *Nanotechnology* **19** 415102
[12] Zhang Q, Lee I, Joo J B, Zaera F and Yin Y 2013 *Acc. Chem. Res.* **46** 1816
[13] Gawande M B, Goswami A, Asefa T, Guo H, Biradar A V, Peng D L, Zboril R and Varma R S 2015 *Chem. Soc. Rev.* **44** 7540
[14] Dhas N L, Raval N J, Kudarha R R, Acharya N S and Acharya S R 2018 Core-shell nanoparticles as a drug delivery platform for tumor targeting *Inorganic Frameworks as Smart Nanomedicines* ed A M Grumezescu (Elsevier) ch 9, p 387
[15] Choi J, Burns A A, Williams R M, Zhou Z, Flesken-Nikitin A, Zipfel W R, Wiesner U and Nikitin A Y 2007 *J. Biomed. Opt.* **12** 064007
[16] Meinardi F, Akkerman Q A, Bruni F, Park S, Mauri M, Dang Z, Manna L and Brovelli S 2017 *ACS Energy Lett.* **2** 2368
[17] Ng W L, Lourenço M A, Gwilliam R M, Ledain S, Shao G and Homewood K P 2001 *Nature* **410** 192
[18] Cheng K Y, Anthony R, Kortshagen U R and Holmes R J 2011 *Nano Lett.* **11** 1952
[19] Li B and Liu J 2011 *IEEE Trans. Nanotechnol.* **10** 284
[20] Xiang J, Lu W, Hu Y, Wu Y, Yan H and Lieber C M 2006 *Nature* **441** 489
[21] Tayagaki T, Hoshi Y and Usami N 2013 *Sci. Rep.* **3** 2703
[22] Yamasaka S, Watanabe K, Sakane S, Takeuchi S, Sakai A, Sawano K and Nakamura Y 2016 *Sci. Rep.* **6** 22838
[23] Sahu A and Kumar D 2022 *J. Alloys Compd.* **924** 166508
[24] Roy A, Healey C P, Larm N E, Ishtaweera P, Roca M and Baker G A 2024 *ACS Nanosci. Au* **4** 176
[25] Mantzaris N V 2005 *Chem. Eng. Sci.* **60** 4749
[26] Ding Y, Yamada R, Gresback R, Zhou S, Pi X and Nozaki T 2014 *J. Phys. D: Appl. Phys.* **47** 485202
[27] Lanham S J, Polito J, Shi X, Elvati P, Violi A and Kushner M J 2021 *J. Appl. Phys.* **130** 163302
[28] Hunter K I, Andaraarachchi H P and Kortshagen U R 2021 *J. Phys. D: Appl. Phys.* **54** 504005
[29] Mangolini L and Kortshagen U 2009 *Phys. Rev.* E **79** 026405
[30] Tavares J, Swanson E J and Coulombe S 2008 *Plasma Process. Polym.* **5** 759
[31] Bapat A, Anderson C, Perrey C R, Carter C B, Campbell S A and Kortshagen U 2004 *Plasma Phys. Control. Fusion* **46** B97
[32] Lin H F, Liao S C and Hung S W 2005 *J. Photochem. Photobiol.* A **174** 82
[33] Olevanov M A, Mankelevich Y A and Rakhimova T V 2004 *J. Exp. Theor. Phys.* **98** 287
[34] Xiong Z *et al* 2022 *J. Appl. Phys.* **55** 235202
[35] Kushner M J 1992 *J. Appl. Phys.* **71** 4173
[36] Perrin J, Leroy O and Bordage M C 1996 *Contrib. Plasma Phys.* **36** 3
[37] Kushner M J 2009 *J. Phys. D: Appl. Phys.* **42** 194013
[38] Le Picard R, Markosyan A H, Porter D H, Girshick S L and Kushner M J 2016 *Plasma Chem. Plasma Process.* **36** 941

[39] Plimpton S 1995 *J. Comput. Phys.* **117** 1–19

[40] Dupuy J L, Lewis S P, Stancil P C, Veeraghattam V K, Manrodt K, Shi X, Elvati P and Violi A 2021 *J. Phys. D: Appl. Phys.* **54** 365203

[41] Kortshagen U R, Sankaran R M, Pereira R N, Girshick S L, Wu J J and Aydil E S 2016 *Chem. Rev.* **116** 11061

[42] Xu C, Andaraarachchi H P, Xiong Z, Eslamisaray M A, Kushner M J and Kortshagen U R 2022 *J. Appl. Phys.* **56** 015201

[43] Beaudette C A, Andaraarachchi H P, Wu C C and Kortshagen U R 2021 *Nanotechnology* **32** 395601

[44] Cernetti P, Gresback R, Campbell S A and Konshagen U 2007 *Chem. Vapor Depos.* **13** 345

[45] Thimsen E, Kortshagen U R and Aydil E S 2015 *J. Phys. D: Appl. Phys.* **48** 314004

[46] Thimsen E, Johnson M, Zhang X, Wagner A J, Mkhoyan K A, Kortshagen U R and Aydil E S 2014 *Nat. Commun.* **5** 5822

[47] Gresback R, Hue R, Gladfelter W L and Kortshagen U R 2011 *Nanoscale Res. Lett.* **6** 68